

Designing Strained Interface Heterostructures for Memristive Devices

Sebastian Schweiger, Reto Pfenninger, William J. Bowman, Ulrich Aschauer, and Jennifer L. M. Rupp*

Material heterostructures have provided discoveries and excitement to engineer novel electro-chemo-mechanic properties for fast ion conductors under strain.^[1–7] Ion conductors and modulating their transport properties are of paramount importance for applications like energy, information technology or sensors, requiring high functional density and properties tailored for the application.^[8–10] This challenges scientists to develop new tools and routes to provide the means to precisely control the material architectures.

The constituents of ion conductor heterostructures can be defined as two oxide materials that are consecutively stacked at varying layer count and layer thickness and grown with a given orientation on a single-crystalline substrate. The resulting lattice mismatch at the interfaces leads to compressive and tensile strain in the two constituent materials, respectively. Choosing one of the materials to be a conductive phase allows the active modulation of the oxygen ionic transport dependent on the magnitude of interfacial strain through the number of interfaces at a constant total film thickness.^[11–13] Up to now, most of the studies in this area have been directed toward a

fundamental understanding without device integration and performance design. However, strained heterostructure oxides may offer a direct integration as functional thin film compounds with tunable carrier transport for novel circuit elements with extended functionalities in the future.

In the last few years the field of ionic memristive memories (also often referred to as memristors or resistive switches) rapidly emerged and received considerable attention due to their potential to replace electronic transistor based technology in future memory and computing architectures.^[14–18] This is because ionic memristive devices offer lower power consumption, shorter read/write times, superior endurance, etc., compared to conventional technologies.^[14] Redox-based memristive memories rely on the control of ionic carriers in oxide thin films under a strong bias stimulus.^[19–21] Despite the huge progress made in the field of memristive memories, material design criteria and tools still need to be developed to open new avenues for material architectures. Here, alternative ways of designing these oxide film structures to alter their carrier flux/concentration profiles under bias for ionic memristive devices to modulate the property of “memristance” are needed. Nowadays, most devices are based on a single oxide film, either crystalline or amorphous,^[22] as the switching element, relying only on doping to control material properties.

For modulating the charge transport, strain engineering is a promising material design tool. It has been shown that strain modulation can alter the resistivity by several orders of magnitude, and can induce large changes in the activation energy when compared to classic doping approaches.^[2,3] Although the impact of strain modulation in ionic heterostructure oxides is clearly demonstrated, no study has been carried out as to how ionic transport-strain modulation affects, on the one hand, the property of “memristance,” and also the performance in a real device. Here, the question of how to design material heterostructures and integrate them into strained ionic memristive devices is explored for the first time for the property of memristance.

To rationally connect the control of strain at heterostructure interfaces to charge transport and memristance, it is necessary to gradually increase the overall strain through an increased number of interfaces, while keeping the ceria-to-erbium ratio and the total film thickness constant. Any such model system must consist of a switching oxide heterostructure sandwiched laterally between two metal electrodes at reasonably small distances in order to achieve the required electric field strength, which is one of the fundamental requirements of the memristive device. This forms the basis to systematically design strained model ionic heterostructures to modulate the physical property

S. Schweiger, R. Pfenninger, W. J. Bowman,
Prof. J. L. M. Rupp
Electrochemical Materials
ETH Zürich
HPP P 21, Honggerberggring 64
8093 Zürich, Switzerland
E-mail: jrupp@mit.edu

W. J. Bowman
School for Engineering of Matter
Transport and Energy
Arizona State University
Tempe, AZ 85287, USA

W. J. Bowman
Laboratory for Electrochemical Interfaces
Massachusetts Institute of Technology
Cambridge, MA 02139, USA

Prof. U. Aschauer
Materials Theory
ETH Zürich
8093 Zürich, Switzerland

Prof. U. Aschauer
Department of Chemistry and Biochemistry
University of Bern
3012 Bern, Switzerland

Prof. J. L. M. Rupp
Electrochemical Materials
Department of Materials Science and Engineering
Massachusetts Institute of Technology
Cambridge, MA 02139, USA



DOI: 10.1002/adma.201605049

of memristance. Reference^[23] reported through a microdot contacting route the successful contacting and strain engineering of heterostructures to measure its impact on “resistance” for the system $Gd_{0.1}Ce_{0.9}O_{2-\delta}/Er_2O_3$. On the other hand, memristive devices are operated at room temperature with high electric fields, conditions under which strain effects are expected to affect ionic conduction most strongly.^[21,24,25] However, devices based on strained ionic conducting oxide heterostructures to alter “memristance” still do not exist, require novel fabrication routes at smaller dimensions compared to state-of-the-art microdots, and principles are still to be proven.

We use lattice strain modulation as a new design tool in oxide heterostructures to gain fundamental insights on the control of oxygen ionic transfer, and to expand our knowledge significantly beyond the previously studied implication on the property of resistance,^[23] newly through this work, to the physical property of “memristance.” This could enable a novel ionic type of electrochemical device, namely, the strained ionic memristor based on oxide heterostructures. In the present study, we carry out a systematic investigation of structural and transport properties of compressively strained microdot heterostructure oxides to design a well-described model system and relate to the newly suggested operation as strained memristive memory through alteration of memristance.

We fabricate biaxially strained heterostructure oxide microdots to study the influence of strain on oxygen anionic switching and the memristive behavior, **Figure 1a**. The microdots are fabricated using pulsed laser deposition (PLD), ablating thin films onto single crystalline sapphire substrates. Our thin film model system consists of two different materials, $Gd_{0.1}Ce_{0.9}O_{2-\delta}$ and Er_2O_3 . One material, in our case $Gd_{0.1}Ce_{0.9}O_{2-\delta}$, is more conductive than the second one by several orders of magnitude.^[26,27] The second material serves in this case only to impose compressive lattice strain on the conductive $Gd_{0.1}Ce_{0.9}O_{2-\delta}$ phase and to therefore modulate the electrical transport in the heterostructure, **Figure 1b**. This strain-imposing phase, here Er_2O_3 , is chosen to be an electrical insulator.^[28] The two phases, conductive and insulating, are stacked consecutively; the total film thickness was kept constant at a thickness of $275\text{ nm} \pm 10\%$, while the number of interfaces was actively varied, that is, from 6 to 60 interfaces. As a result, the heterostructure oxide microdots with a low number of interfaces are supposed to have less strain acting on the ionic conductor lattice and interfacial strain increases with an increasing number of interfaces for the microdot, since the strain is the biggest at the interfaces. Now to rationally access the strained interfaces down to nanoscale, it is necessary to develop a unique device design with sideways attached electrodes contacting the free-etched heterostructure dots on a chip. The switching mechanism for ceria-based memristive devices is based on oxygen vacancy conduction in the ion conductor balanced by electronic carriers,^[27,29,30] which we will now actively tune by imposing the strain field in various degrees with the insulating erbia layer and monolayer thickness variations in the heterostructure dot device. Herein, to operate the device units on the chip newly as memristors it is a prerequisite to apply high electric field strengths, in the range of $MV\ m^{-1}$, for operation as memristive memory. In order to achieve this, a substantial reduction in the device size relative to previously reported microdot devices^[23] was necessary. Hence,

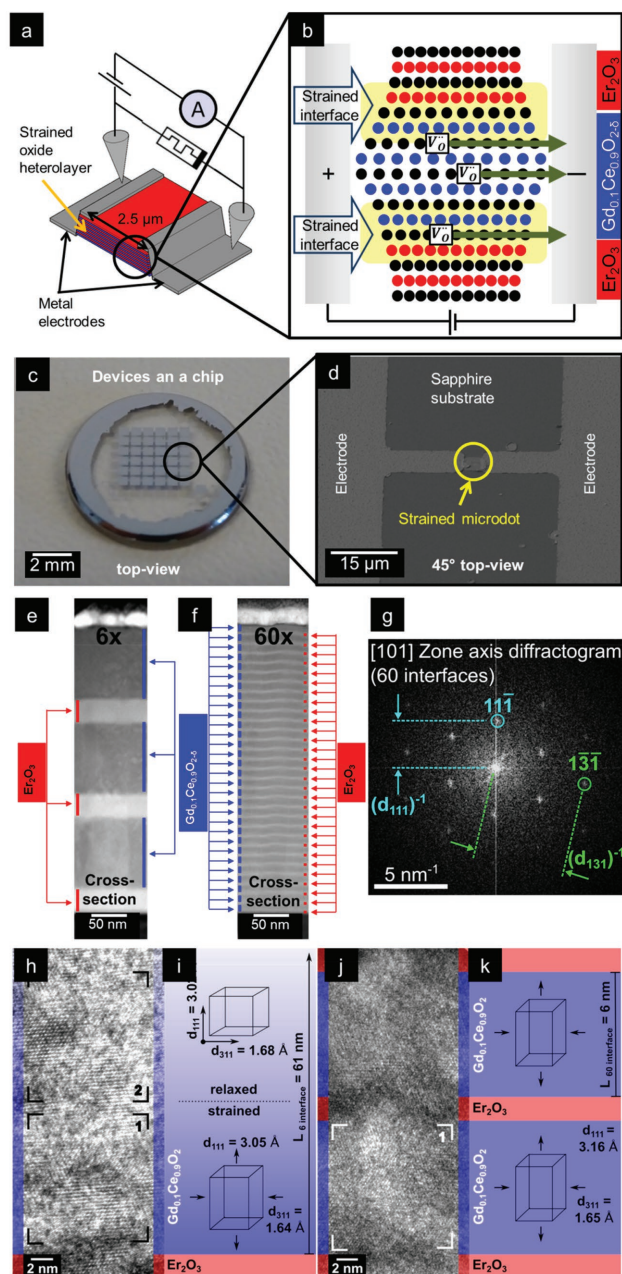


Figure 1. Strained multilayer microdots. a) Schematic view of the microdot system. b) Schematic view of one of the $Gd_{0.1}Ce_{0.9}O_{2-\delta}/Er_2O_3$ interfaces illustrating the use of interfacial lattice mismatch to generate strain and the applied conduction model. c) Optical image of the electrode arrangement on the chip with the ceramic microdots in between the contacting bridges. d) SEM image of the strained microdot on the chip. e, f) Annular dark field STEM cross-sectional view of a 6 and 60 interfaces $Gd_{0.1}Ce_{0.9}O_{2-\delta}/Er_2O_3$ multilayer sample, respectively. g) Diffractogram of $Gd_{0.1}Ce_{0.9}O_{2-\delta}$ layer displaying fluorite structure (computed from region 1 in (h)). h, i, j) Bright field HRTEM images of $Gd_{0.1}Ce_{0.9}O_{2-\delta}/Er_2O_3$ interface(s) in 6 and 60 interface samples, respectively, with highlighted regions labeled “1” and “2” indicating the areas used to compute diffractograms. i, k) Diagram illustrating the results of the Miller plane spacing measurements in the out-of-plane and in-plane directions in the conducting oxide phase. The six interface sample contains a more relaxed region “2” positioned 12 nm from the interface, and a more strained region “1” adjacent to the interface, whereas the conducting phase in the 60 interface sample is fully strained, k.

the challenge to realize these high field strengths and to contact the strained interfaces directly through sideways attached electrodes at small distances had to be overcome. In this work, we present successfully contacted microdot switching structures to alter “memristance” with a small size of $\approx 2.5 \mu\text{m}$ diameter, Figure 1c,d. Importantly, this is now roughly a one order of magnitude decreased microdot size when compared to the state-of-the-art in literature which was previously used to alter “resistance”^[23] and is an important step to realize those new memristive switches under strain. These microdots were fabricated using photolithography and physical dry-etching, to obtain devices at micrometer scale, see Experimental Section and Section S1 (Supporting Information) for details on the microfabrication process flows and materials etch rates.

High-resolution transmission electron microscopy (HRTEM) imaging and diffraction techniques have been successfully employed to investigate oxide heterolayers, such as Fourier analysis of high-resolution images to investigate crystallographic orientation relationships at heterolayer interfaces. Here, we apply both TEM and scanning transmission electron microscope (STEM) imaging and diffraction analyses to assess heterostructure layer growth, and the strain state of the conducting oxide phase. In cross-sectional annular dark field STEM images, we observe well-defined layers of $\text{Gd}_{0.1}\text{Ce}_{0.9}\text{O}_{2-\delta}$ and Er_2O_3 stacked consecutively with monolayer thicknesses down to 3 nm, Figure 1e,f. Oriented growth of the multilayer heterostructure using sapphire substrates allows for well-defined interfaces between the two materials, which we demonstrate on two examples using HRTEM imaging for the 6 and 60 interface modulated heterostructure oxides in a microdot. In PLD grown material systems columnar growth can be observed. This implies that at the phase boundaries between the materials interfaces of high quality can be obtained, but in the system there are still grain boundaries present. While keeping the total device thickness constant, the number of interfaces is being increased. This results in an increase of the strain-affected volume over the total device. The growth conditions employed here result in oriented growth of columnar grains in the out-of-plane [111] direction. The influence of different growth rates for $\text{Gd}_{0.1}\text{Ce}_{0.9}\text{O}_{2-\delta}$ and Er_2O_3 can also be observed in the cross sections, see also Section S1 (Supporting Information) for deposition rates, Table S1.1 (Supporting Information). Diffraction analysis reveals that the cubic fluorite structure^[31] is present throughout the heterostructure microdots for the

$\text{Gd}_{0.1}\text{Ce}_{0.9}\text{O}_{2-\delta}$ phases, Figure 1g. Following a similar TEM diffraction approach to strain mapping in confined Si thin films,^[32] Fourier analysis of HRTEM images was used to make a relative assessment of lattice distortion in the conducting ceria phase for the 6 and 60 interface modulated samples.

Miller plane spacings, d_{hkl} , in the out-of-plane [111] direction and the approximately in-plane [311] direction were measured in the $\text{Gd}_{0.1}\text{Ce}_{0.9}\text{O}_{2-\delta}$ phases of the heterostructure microdots using diffractograms (e.g., Figure 1g and Section S2, Supporting Information). Diffractograms, like selected-area electron diffraction patterns, provide a reciprocal space representation of the lattice fringes visible in an HRTEM image as an array of diffraction spots. Diffractograms were computed here by Fourier transforming the highlighted regions labeled “1” and “2” in the HRTEM images, see Figure 1h,j for 6 and 60 interfaces, respectively. The highlighted regions are $\approx 11 \text{ nm}$ tall (i.e., in the direction normal to the $\text{Er}_2\text{O}_3/\text{Gd}_{0.1}\text{Ce}_{0.9}\text{O}_{2-\delta}$ interface), with region “2” in the six interface heterostructure microdot positioned 12 nm from a heterolayer interface. For the six interface heterostructure we assumed region “2” to be more relaxed, as it is furthest from an interface. Importantly, compared to region “2” in the six interface sample, the 60 interface sample exhibits elongation in the out-of-plane (111) spacing by $4.5 \pm 0.2\%$, which is accompanied by a contraction in the in-plane (311) spacing by $2.1 \pm 0.2\%$. This is consistent with interfacial compressive strain in region “1” of the 60 interface sample. In contrast, when compared to region “2” in the six interface sample (12 nm from the interface), the out-of-plane (111) spacing in region “1” (adjacent to the interface) is only elongated by $1.2 \pm 0.2\%$. In conclusion, we report fully strained $\text{Gd}_{0.1}\text{Ce}_{0.9}\text{O}_{2-\delta}$ layers for the 60 interfaces microdot with in-plane compression, and in contrast, relaxation toward the center of the $\text{Gd}_{0.1}\text{Ce}_{0.9}\text{O}_{2-\delta}$ layers for the six interfaces microdot. This analysis is detailed in Table 1. The oriented growth was further confirmed by XRD, see Section S3 (Supporting Information).

To understand if Gd segregation at the interfaces could play a role in modulating the memristance, we investigated the $\text{Gd}_{0.1}\text{Ce}_{0.9}\text{O}_{2-\delta}$ cation distribution in the $\text{Gd}_{0.1}\text{Ce}_{0.9}\text{O}_{2-\delta}/\text{Er}_2\text{O}_3$ interface region of an as-prepared heterolayer sample via electron energy-loss spectroscopy (EELS) in a STEM, see Section S4 (Supporting Information). $\text{Gd}_{0.1}\text{Ce}_{0.9}\text{O}_{2-\delta}$ spectra acquired near the $\text{Gd}_{0.1}\text{Ce}_{0.9}\text{O}_{2-\delta}/\text{Er}_2\text{O}_3$ interface (within 2.5 nm) and relatively far from the interface (22–28 nm) were compared

Table 1. Comparison of $\text{Gd}_{0.1}\text{Ce}_{0.9}\text{O}_{2-\delta}$ out-of-plane and in-plane Miller spacing obtained through TEM and out-of-plane strain obtained through Raman spectroscopy.

Microdot constituents	No. of interfaces microdot		Region	TEM d_{111} [Å]	TEM d_{311} [Å]	Raman F_{1g} (out-of-plane) strain [%]
$\text{Gd}_{0.1}\text{Ce}_{0.9}\text{O}_{2-\delta}/\text{Er}_2\text{O}_3$	6 (Figure 1h)		2	3.02 ± 0.06	1.68 ± 0.02	0.0085
$\text{Gd}_{0.1}\text{Ce}_{0.9}\text{O}_{2-\delta}/\text{Er}_2\text{O}_3$	6 (Figure 1h)		1	3.05 ± 0.04	1.64 ± 0.01	0.0085
$\text{Gd}_{0.1}\text{Ce}_{0.9}\text{O}_{2-\delta}/\text{Er}_2\text{O}_3$	60 (Figure 1j)		1	3.16 ± 0.05	1.65 ± 0.01	0.61

to determine if there was a significant difference in the ratio of intensities of the cerium (Ce M_{45}) to gadolinium (Gd M_{45}) signals, which is proportional to the ratio of elemental concentrations.^[33] The difference in measured intensity ratios in the layer and interface regions was found to be negligible within the measurement error in this case, indicating that the two regions exhibit approximately equal area-averaged cation stoichiometry, see Figure S4.1 (Supporting Information) for details. Therefore, it is reasonable to conclude that cation segregation does not play a role in the strain and interface-induced modification of the overall memristive response in these heterostructure devices. EELS also indicated that Ce ions in the interface region were reduced relative to Ce ions in the layer region, a consequential point discussed below and in Section S4 (Supporting Information).

We successfully present a novel design strategy for the heterostructure microdots, which are deployable for testing as switching device to alter memristance. We analyze the strain state near the interface and in the relaxed zones by HRTEM, showing the evolution of strain relaxation within the thin film and the in-plane and out-of-plane strain anisotropy. This allows us to locally resolve the strain states at the interfaces and in the center of the layers. In the following we investigate the influence of interface modulations on structure and the property of memristance.

Motivated by the opportunity to modulate the interfacial strain through the number of interfaces and monolayer thickness for the $Gd_{0.1}Ce_{0.9}O_{2-\delta}/Er_2O_3$ heterostructure unit in the device architectures, we turn to Raman microscopy to probe the atomistic near-order correlations and provide a first Raman mapping relative to the device structure features and vibrational modes, **Figure 2a**. We use cluster analysis to decompose the hyperspectral map into single clusters, which can be assigned to the materials and device segments, **Figure 2b,c**.

Raman spectroscopy is a particularly useful type of vibrational spectroscopy to investigate such systems, as exemplified by Kreisel et al.,^[34] for the following reasons: First, we excite the interactions between the cation- and anion sublattices which makes this technique particularly sensitive to changes in the oxygen sublattice.^[35] Since the ionic transport in the conductive phase of $Gd_{0.1}Ce_{0.9}O_{2-\delta}$ relies on the oxygen sublattice, this allows us to draw conclusions about structure–transport interactions. Second, we can measure with high spatial resolution (≈ 360 nm),^[36] which is useful for measuring our micrometer-sized devices using a 532 nm laser for excitation. Unlike TEM, Raman spectroscopy directly probes the full extent of the thin film sample in out-of-plane direction. Third, it allows us to directly study the strain states at the interface through interpretation and analysis of the change in the ionic bond strengths through the shift of the frequencies of the Raman bands. When a bond of a heterostructure oxide phase is stretched or compressed it changes its vibrational frequency, thereby altering the peak position of the respective mode. Analyzing the Raman spectra, **Figure 2d**, we first turn to the reference sample made from pure $Gd_{0.1}Ce_{0.9}O_{2-\delta}$ in a single thin film microdot device. A single Raman-active peak is visible, originating from the unstrained fluorite structure for only one triply degenerate F_{2g} mode, in agreement with literature.^[37,38] The efficiency of scattering I is given by

$$I = C \sum_j |e_i R_j e_s|^2 \quad (1)$$

where C is a constant, R_j is the Raman tensor of a phonon j , and e_i and e_s are the polarization vectors of the incoming and scattered beams, respectively. For $Gd_{0.1}Ce_{0.9}O_{2-\delta}$ fluorite structure-type the Raman tensors for the three directions of the crystal coordinate system are given by

$$R_x \begin{bmatrix} 0 & 0 & 0 \\ 0 & 0 & d \\ 0 & d & 0 \end{bmatrix}, R_y \begin{bmatrix} 0 & 0 & d \\ 0 & 0 & 0 \\ d & 0 & 0 \end{bmatrix}, R_z \begin{bmatrix} 0 & d & 0 \\ d & 0 & 0 \\ 0 & 0 & 0 \end{bmatrix} \quad (2)$$

In the absence of stress the three optical Raman modes have the same frequency of about 464 cm^{-1} as the isotropic cubic crystal system is from a group theoretical point of view symmetry inverse, see Loudon for details.^[39] In the spectra of the $Gd_{0.1}Ce_{0.9}O_{2-\delta}/Er_2O_3$ heterostructure microdots we can observe a peak splitting of the triply degenerated F_{2g} mode into the in-plane F_{2g} and the out-of-plane F_{1g} modes related to strained $Gd_{0.1}Ce_{0.9}O_{2-\delta}$ cubic fluorite structure, **Figure 2e** and inset of **Figure 2g**. Usually Raman modes denoted A or B represent singly degenerate modes, E doubly degenerate modes, and F (or T) triply degenerate modes. Here, the peak splitting is denominated F_{2g} and F_{1g} to improve the traceability. The splitting of the triply degenerate F_{2g} mode is associated with a decrease of symmetry for biaxially strained samples where the isotropy between in-plane and out-of-plane direction is lifted.^[40–42] The strain analysis through Raman microscopy is focused on the $Gd_{0.1}Ce_{0.9}O_{2-\delta}$ modes, since this is the phase that is relevant for the transport behavior, that is, all current flows through this phase. Importantly, this finding agrees with the observation in TEM where we see the elongation along the out-of-plane axis, more pronounced with increasing in-plane compression, as detailed in **Figure 1h–k** and **Table 1**. This lifting of the symmetry could also influence Poisson's ratio.^[43] Information on erbia Raman spectra assignment is presented in detail in Section S6 (Supporting Information).

We observe a monotonic shift of the relevant Raman band with an increase in the number of interfaces for the $Gd_{0.1}Ce_{0.9}O_{2-\delta}/Er_2O_3$ heterostructure dots, **Figure 2f**. The strain is largest at the interface and relaxes toward the interior of the layers, this means when we start to decrease the monolayer thickness at a constant total film thickness for the $Gd_{0.1}Ce_{0.9}O_{2-\delta}$ phase, the strain fields can relax less, leading to an overall increase of strain in the system and the splitting of the F_{2g} Raman mode is most pronounced. *Viz.*, this agrees with the TEM analysis, **Figure 1h–k**. The strain associated with the frequency shift is computed through density functional theory (DFT) calculations. Frequencies of the Raman-active stretching modes were computed in the fluorite unit cell with different amounts of imposed in-plane strain, **Figure 2g**. The underestimation of the Raman frequencies in the calculations can be explained by the missing larger Gd ions, which are expected to blue shift the frequencies. The magnitude of relative changes as a function of strain is, however, expected to be reliably predicted. Using the values obtained thereby, we were able to calculate strains in the $Gd_{0.1}Ce_{0.9}O_{2-\delta}$ phase ranging from relaxed (unstrained) to -1.26% compressive strain for 60 interfaces

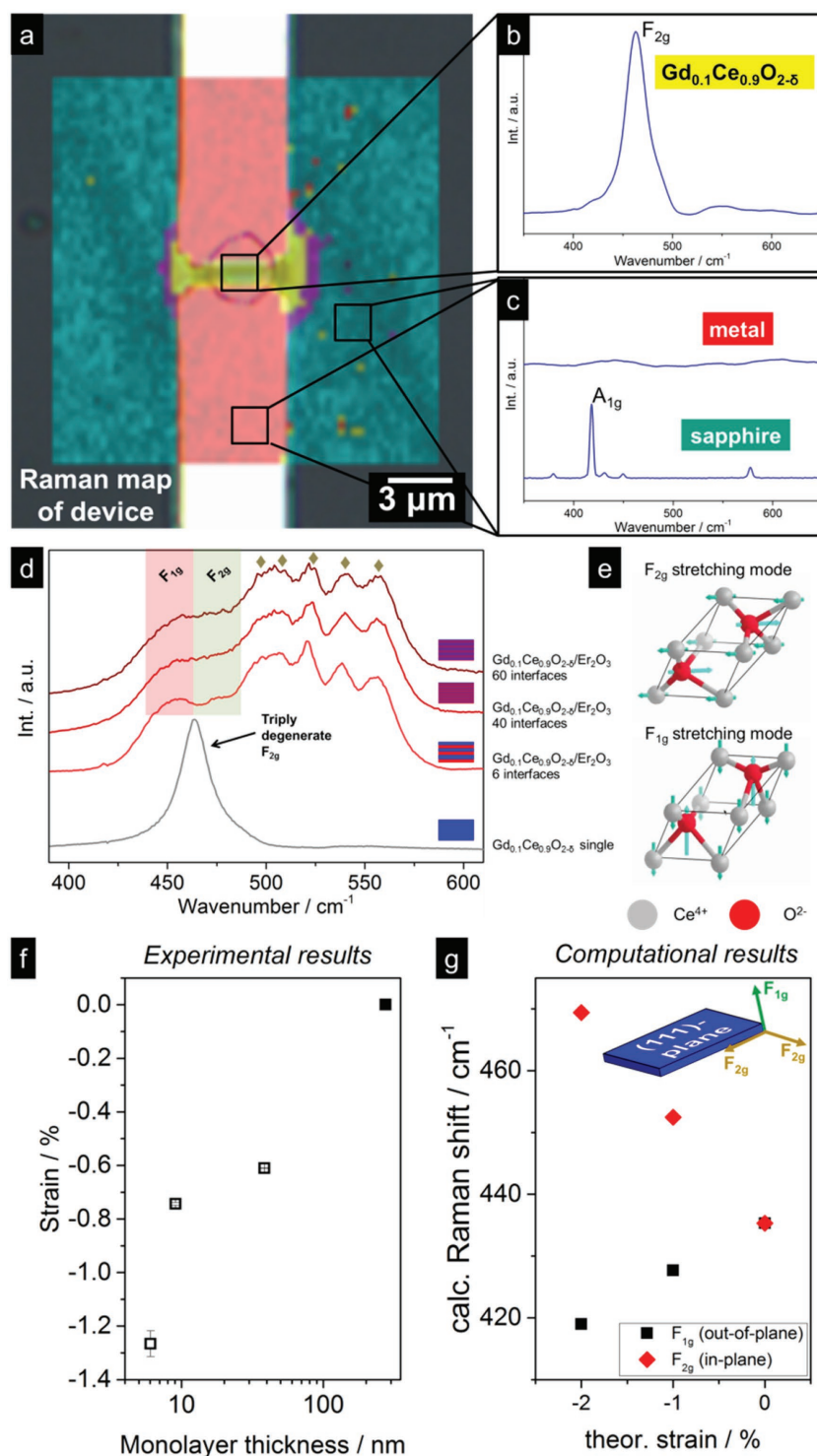


Figure 2. Structural characterization, mapping, and interfacial strain state. a) Raman device map to investigate the structural consistency of the microdots. The yellow, red, turquoise, and purple colors represent different materials obtained through cluster analysis. The purple rim represents an overlay of the yellow $\text{Gd}_{0.1}\text{Ce}_{0.9}\text{O}_{2-\delta}$ signal and the turquoise sapphire signal. b) Cluster analysis of Raman modes extracted from the Raman device map showing the $\text{Gd}_{0.1}\text{Ce}_{0.9}\text{O}_{2-\delta}$ single phase device. c) Cluster analysis of Raman modes extracted from the Raman device map showing the electrodes and the substrate, respectively. d) Micro-Raman spectra of the compressively strained microdots. F_{2g} and F_{1g} denote the relevant cationic–anionic $\text{Gd}_{0.1}\text{Ce}_{0.9}\text{O}_{2-\delta}$ Raman bands. The diamonds represent Er_2O_3 bands. The $\text{Gd}_{0.1}\text{Ce}_{0.9}\text{O}_{2-\delta}$

heterostructure microdots. We want to point out that these strain values obtained via DFT calculations are in good agreement (within $\pm 0.1\%$) with strain values obtained by high-pressure Raman studies on ceria crystals.^[44] For further information on how to analyze Raman scattering data from strained samples see Section S5 (Supporting Information).

Local Raman mapping was successful and used for the first time on a heterostructure microdot device to probe memristance in connection with DFT computations to access the strain states and to show anisotropy present in the conductive $\text{Gd}_{0.1}\text{Ce}_{0.9}\text{O}_{2-\delta}$ phase of the microdot. Density functional theory predictions were used to analyze the data and relate the experimentally obtained values to compressive strains at the internal interfaces. Results of Raman mapping measurements are consistent with those from aforementioned TEM analysis. We use these results to further study the implication on memristance under strain for the microdot devices.

As an initial step to characterize the transport behavior of our samples, they were subjected to a preforming procedure in accordance with literature.^[45,46] After successful preforming the samples were investigated with cyclic voltammetry, **Figure 3** and **Table 2**. We observe for the single-phase $\text{Gd}_{0.1}\text{Ce}_{0.9}\text{O}_{2-\delta}$ sample that with increasing positive voltage there is a continuous increase in current, **Figure 3a**. Once we have reached the maximum and decrease the voltage again, the current decreases as well with a slight hysteresis. For the negative polarity a similar behavior can be observed. After increasing the current with rising voltage at negative polarity we reach the negative maximum, then we decrease the voltage again and observe a continuous decrease of current until zero voltage is reached. Hence, changing the polarity of the device resets it back to the high resistance state within one switching cycle. The unstrained $\text{Gd}_{0.1}\text{Ce}_{0.9}\text{O}_{2-\delta}$ microdot reveals an asymmetric hysteretic memristive switching curve with a low $R_{\text{off}}/R_{\text{on}}$ ratio of ≈ 1.5 in the positive branch. We ascribe the asymmetry of the

single-phase sample shows the triply degenerate F_{2g} mode. e) Splitting of the $\text{Gd}_{0.1}\text{Ce}_{0.9}\text{O}_{2-\delta}$ bands due to symmetry change in out-of-plane and in-plane modes. f) Analysis of the band shifts using the computational results to compute the magnitude of interfacial strain. g) DFT simulations to correlate the Raman frequency shift to strain states. Inset: Raman mode splitting in the sample reference system.

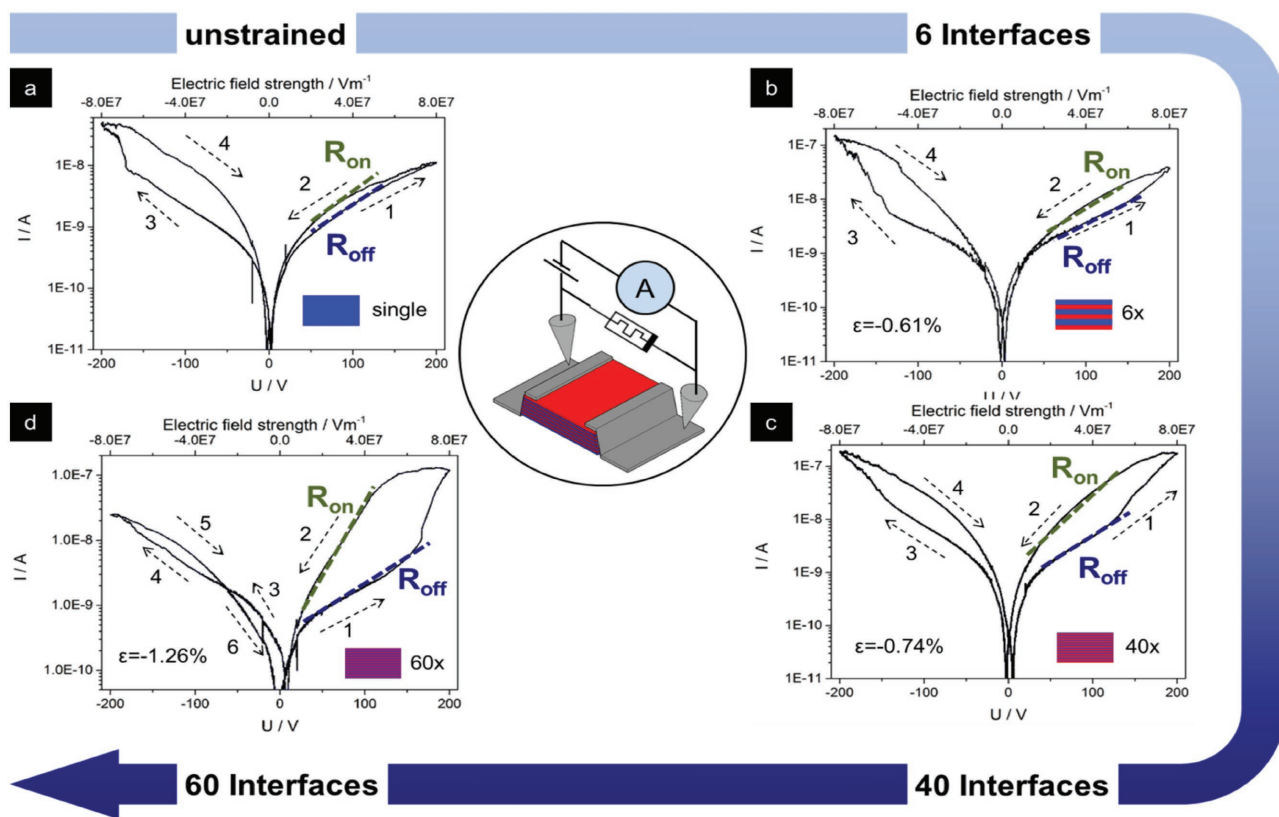


Figure 3. Electrical characterization through cyclic voltammetry and memristive behavior. a) *I*–*V* curve of the unstrained $\text{Gd}_{0.1}\text{Ce}_{0.9}\text{O}_{2-\delta}$ single-phase microdot. b) *I*–*V* curve of the six interfaces sample. c) *I*–*V* curve of the 40 interfaces sample. d) *I*–*V* curve of the 60 interfaces sample with a strain of -1.26% . This curve shows an additional crossing at negative polarity. The $R_{\text{off}}/R_{\text{on}}$ ratio increase from 1.5 to 15 when increasing the compressive strain from unstrained to -1.26% .

current–voltage profile to the initial preforming step applied with positive polarity discussed in ref. [46].

Now increasing the compressive strain on the $\text{Gd}_{0.1}\text{Ce}_{0.9}\text{O}_{2-\delta}$ heterolayer phases of the microdot increases the hysteretic opening at positive polarity while maintaining the volatile switching characteristics, Figure 3b–d. This leads to an increase of the $R_{\text{off}}/R_{\text{on}}$ ratio, see also Table 2. When the compressive strain on the conductor of the heterolayer dot is increased to -1.26% the switching characteristics of the systems are

changing to a nonvolatile behavior, Figure 3d. For the positive branch a further increase of the $R_{\text{off}}/R_{\text{on}}$ ratio can be observed, reaching more than one order of magnitude. Analysis of the microdots’ current–voltage profiles revealed that the OFF-state (high resistance state) remains virtually unchanged with respect to strain at the heterostructure interfaces in the $\text{Gd}_{0.1}\text{Ce}_{0.9}\text{O}_{2-\delta}$ phase, Figure 4a. Importantly, it is the conductivity of the ON-state (low resistance state) of the heterostructure dot device that is being modulated by the effective strain imposed on the

Table 2. Analysis of the *I*–*V* profiles in resistive switching for strained heterolayer microdots.

Microdot constituents	No. of interfaces microdot	$\text{Gd}_{0.1}\text{Ce}_{0.9}\text{O}_{2-\delta}$ monolayer thickness [nm]	Er_2O_3 monolayer thickness [nm]	In-plane strain	$R_{\text{off}}/R_{\text{on}}$ ratio	Persistence
$\text{Gd}_{0.1}\text{Ce}_{0.9}\text{O}_{2-\delta}$ (Figure 3a)	Single phase	275	–	Unstrained	1.48	Volatile
$\text{Gd}_{0.1}\text{Ce}_{0.9}\text{O}_{2-\delta}/\text{Er}_2\text{O}_3$ (Figure 3b)	6	61	30	-0.61%	2.00	Volatile
$\text{Gd}_{0.1}\text{Ce}_{0.9}\text{O}_{2-\delta}/\text{Er}_2\text{O}_3$ (Figure 3c)	40	9	4.5	-0.74%	5.39	Volatile
$\text{Gd}_{0.1}\text{Ce}_{0.9}\text{O}_{2-\delta}/\text{Er}_2\text{O}_3$ (Figure 3d)	60	6	3	-1.26%	14.94	Nonvolatile

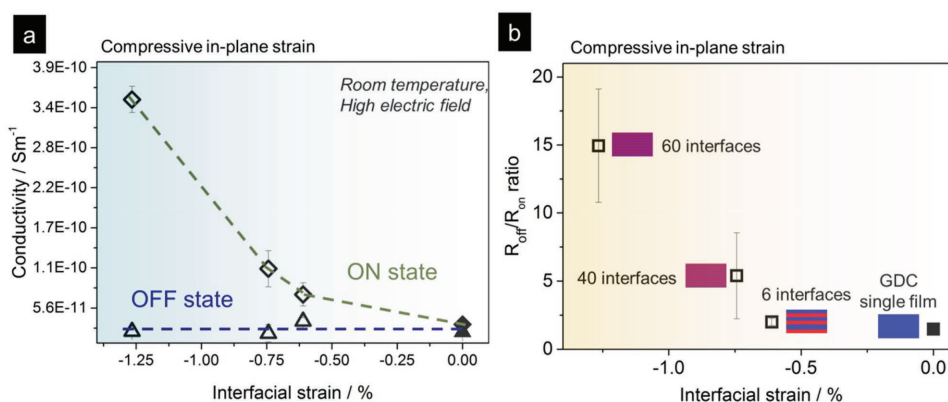


Figure 4. Strained interfaces to control memristance. a) The interfacial state of the system acts primarily on the ON-state, the OFF-state remains unchanged. b) This behavior leads to a minimum $R_{\text{off}}/R_{\text{on}}$ ratio at the unstrained sample and an increased $R_{\text{off}}/R_{\text{on}}$ ratio with an increasing number of interfaces.

$\text{Gd}_{0.1}\text{Ce}_{0.9}\text{O}_{2-\delta}$ phase under the high local electric fields. We report that increasing the effective compressive in-plane strain up to -1.26% in the $\text{Gd}_{0.1}\text{Ce}_{0.9}\text{O}_{2-\delta}$ phase of the heterostructure microdots results in an increase of the $R_{\text{off}}/R_{\text{on}}$ ratio by one order of magnitude, Figure 4b. In the present study, we operate for the first time memristive heterostructure microdots to alter memristance at room temperature under high local electric field strength of about 80 MV m^{-1} and observe for increased strain the enlargement in the assigned $R_{\text{off}}/R_{\text{on}}$ ratio of the switch.

We interpret the finding as follows in light of the atomistic structure investigations by Raman and TEM measurements, Figure 5a,b. Earlier, Gao et al.^[47] investigated the switching behavior of single-phase ceria films through in situ TEM studies, revealing resistive switching by a filamentary-type mechanism, mediated by reduced Ce_2O_3 portions within the ceria films. Also, Song et al.^[48] reported a preferential reduction of ceria at the interfaces within heterostructures formed with zirconia-based oxides as second constituent material. They find that ceria reduction at the interface is independent of the strain, since the Ce^{3+} concentrations are identical for compressive and strain fields applied. However, DFT studies showed that under compressive strain both neutral (i.e., thermally created) and ionized (i.e., charge-compensating for Gd^{3+} dopants) oxygen vacancies prefer to be located at the $\text{Ce}_2\text{O}_3/\text{ZrO}_2$ interface.^[49] Such a cerium reduction at the interface is consistent with our own EELS observations, and we confirm the latter results for the $\text{CeO}_2/\text{Er}_2\text{O}_3$ interface based on our own DFT computation where we plot the energy as a function of the distance to the interface, Figure 5c. Additional information to the DFT calculations of vacancies at the $\text{CeO}_2/\text{Er}_2\text{O}_3$ interface is presented in Section S7 (Supporting Information). Together with our own structural TEM, EELS, and Raman investigations, we propose that reduction of ceria takes place close to the (strained) interfaces, increasing the interfacial Ce^{3+} concentration during preforming under high electric field strength in our heterostructure microdot devices for memristance modulation. This is comparable to reduction effects of PLD-grown ceria layers relative to the air interface that are described by Chueh et al.^[50] using XPS. See Section S8 (Supporting Information) for detailed defect chemical equations on the ceria reduction at the strained interfaces.

We now turn to the effect of the systematically modulated strained volumes in the ceria-based phases of the heterostructures on the memristive response: By two independent structural investigation methods, TEM and Raman, Figures 1 and 2, we show that the magnitude of strain and, importantly, of its biaxial lattice distortion is systematically increased with increasing number of interfaces in the microdot, Table 1. Second, in the heterostructure dots with a low interface count, a relaxed and less biaxially distorted zone is found within the ceria-based monolayer structures for distances greater than 12 nm from the interface. The overall higher degree of biaxial lattice distortions in the ceria-based heterostructure dots with 60 interfaces (high strain) has an effect on both the ionic and electronic charge carriers and the mixed conductivity. A formation energy reduced by up to several tenths of eV^[49] results in an increased effective concentration of oxygen vacancies also balanced by an increased number of electronic carriers (in line with our EELS observations).^[48,50] The oxygen vacancy mobility is reduced due to increased migration barriers under compressive strain^[13] as also confirmed by our DFT calculations (Section S7, Supporting Information). Here, the curvature of the lowest unoccupied bands in pure CeO_2 is found to increase with increasing compressive strain, meaning that the electrons resulting from oxygen vacancy formation, which reside in these bands, are characterized by a lower effective mass and hence higher mobility with increasing compressive strain, Figure 5d. For the highly strained (high interface count) microdot heterostructures, the high biaxial strain thus leads to an increase in the electronic mobility that can be used for modulation of the memristance in the ON-state. The excess electrons created populate the Ce 4f band.^[51] The overall conductivity is given by

$$\sigma_{\text{tot(RT,highE,totalV)}} = \mu_e \times [e'] \times q + \mu_{\text{VO}} \times [V_{\text{O}}] \times (2q) \quad (3)$$

where σ_{tot} stands for the total conductivity over the total volume of the $\text{Gd}_{0.1}\text{Ce}_{0.9}\text{O}_{2-\delta}$ phase of the device. μ_e and μ_{VO} represent the electronic and ionic mobilities, respectively; $[e']$ and $[V_{\text{O}}]$ are the electronic and ionic charge carrier densities and q represents the elementary charge. The modulation of the electronic charge carrier densities balanced by oxygen ionic vacancies and their mobilities, respectively, gives rise to the memristance

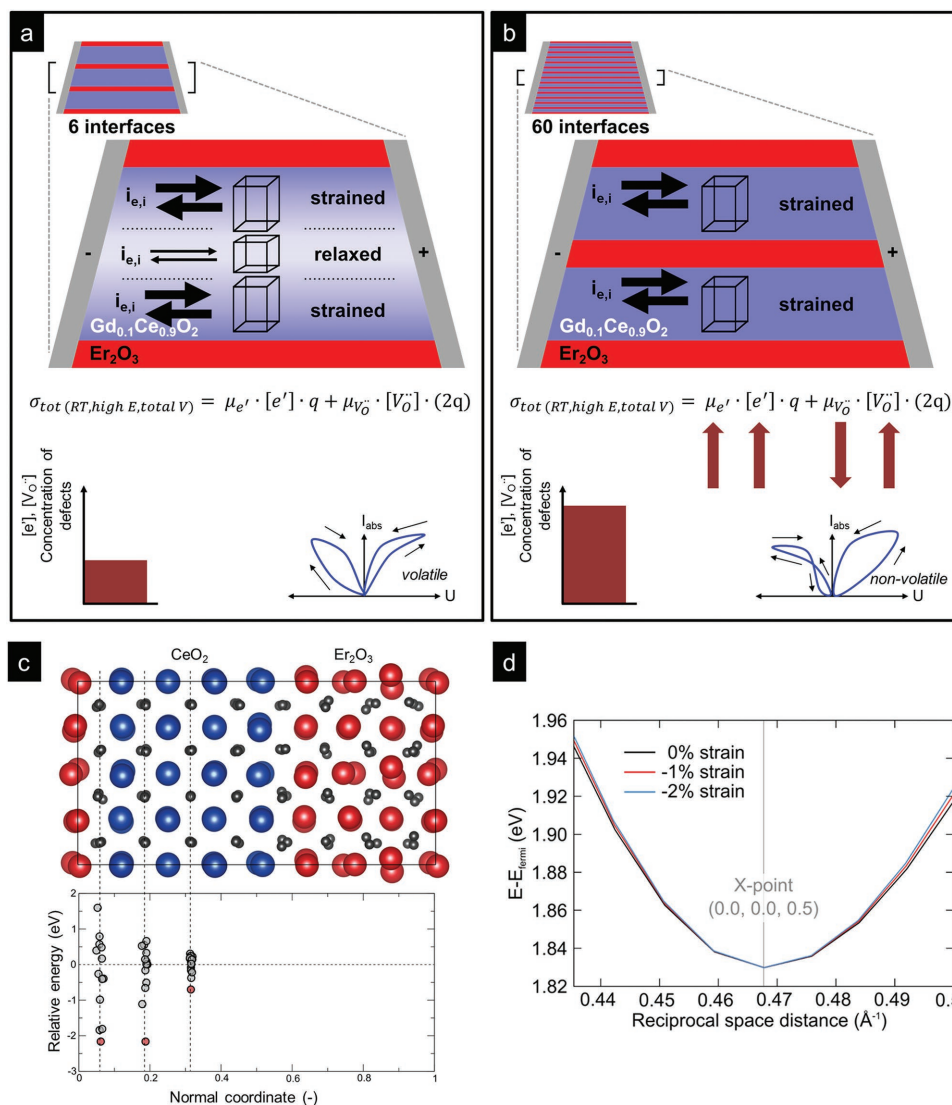


Figure 5. Reduced interfacial states in heterostructures. a) The strained interfaces give rise to an increase in the number of charge carriers. The compressively strained volumes decrease the mobility of the oxygen ions. In samples with a low number of interfaces the strain relaxes toward the center of the $\text{Gd}_{0.1}\text{Ce}_{0.9}\text{O}_{2-\delta}$ phase, decreasing the fraction of strained material with respect to the total device volume. The total conductivity is given by $\sigma_{\text{tot}}(\text{RT,high } E, \text{total } V) = \mu_{e'} \times [e'] + \mu_{V_O} \times [V_O]$, where σ_{tot} stands for the total conductivity over the total volume of the $\text{Gd}_{0.1}\text{Ce}_{0.9}\text{O}_{2-\delta}$ phase of the device. $\mu_{e'}$ and μ_{V_O} represent the electronic and ionic mobilities, respectively; $[e']$ and $[V_O]$ are the electronic and ionic charge carrier densities. b) In samples with a high number of interfaces the device volume is fully strained. The influence on charge carrier densities and mobilities is much larger. c) DFT calculations show it is energetically favorable for the defects to be located close to the interfaces. d) Increasing the compressive strain reduces the effective mass of the electrons, thereby increasing the electronic mobility, as confirmed through DFT calculations.

modulation after preforming. This interplay of electronic and ionic conductivity also explains the change of persistence in highly strained and high interface count samples. At low temperature conditions the conductivity is predominantly electronic.^[52,53] The increase in memristance, that is, the formation of the hysteresis during cycling is a product of the changed conductivities, due to the formation of reduced filaments of ceria during the bias sweep at the phase boundary with erbia,^[47] facilitated through the interfaces^[48] and modulated by the compressive in-plane strain. The introduction of the additional crossing in the current-voltage signal of the high interface count sample can be explained through the mechanism of filament breakdown: When the maximum voltage is reached and the bias is

swept back to zero, the filament of reduced material is reoxidized through transport of oxygen ions to the filamentary-type interfacial portion of Ce^{3+} . This ionic transport is governed by compressive strain, and as a consequence slowed down, because oxygen ions must diffuse inward from the electrodes or the edge of the device. Only if the ionic transport is very slow (i.e., in devices with a high level of compressive strain) the filament is stable enough to keep the kinetically frozen low resistance state while cycling back to zero voltage and then start cycling with opposite polarity. Another reason supporting these characteristics is the overall change in relaxed (nonreduced) volumes as confirmed in our HRTEM measurements. Samples with a lower interface count have thicker individual

$\text{Gd}_{0.1}\text{Ce}_{0.9}\text{O}_{2-\delta}$ layers; therefore, more material is available which acts as oxygen reservoir.^[54] A varying magnitude of strain in the $\text{Gd}_{0.1}\text{Ce}_{0.9}\text{O}_{2-\delta}$ phases and interfacial effects altered by the interface count in the heterostructure microdots of the devices structurally govern the break in cubic symmetry, raising oxygen vacancy sites and in turn, can be actively used to tune the memristance property.

The results show a new, exciting way to use multilayered heterostructure oxides as a functional building block to control the degree of biaxial strain in ionic conductors, and demonstrate for the first time their direct implication for devices with tuned memristive properties by strain. The resistive switching and memristive behavior could be changed from volatile to nonvolatile memristance upon strain modulations in the conducting phase of the heterostructure oxide units on the example of $\text{Gd}_{0.1}\text{Ce}_{0.9}\text{O}_{2-\delta}/\text{Er}_2\text{O}_3$ materials. The successful decrease of the microdot size by one order of magnitude compared to state-of-the-art in literature to reach an electrode separation of 2.5 μm , yielding electric field strength of up to 80 MV m^{-1} , allowed accessing the property of “memristance” for strained multilayer heterostructures. The systematic and successful increase of strained volume in the $\text{Gd}_{0.1}\text{Ce}_{0.9}\text{O}_{2-\delta}$ phase of the heterostructure microdots was proven by Raman microscopy together with DFT simulations to interpret the experimental results. Raman imaging was used as a novel method to locally relate the chemical mapping of the material and strain states to the device structure. The results obtained by Raman microscopy and complementary TEM analysis clarify that local strain relaxation could be observed within the low interface count sample in the conducting phases of the heterolayer dots. We reveal that for the high number of interfaces, tuning the repetitions of ceria and erbia layers down to 3 nm, the increased biaxial strain distortion results not only in a modulation of the ionic conductivity primarily through the changed migration barriers, but also the electronic mobility via strain-induced enhanced electronic mobility. Furthermore, the defect concentration at the interfaces is increased with greater strain levels. We provide a successful integration and design of strain levels and lattice biaxial distortion to tune the charge carrier transport in an ionic heterostructure oxide, and demonstrate their direct implication as novel microdot devices to modulate the property of memristance. The presented materials design concepts and insights are useful to make new architectures for micro-electrochemical devices beyond classic doping strategies, not only for digital information storage applications based on memristance but also for related fields such as energy harvesting and storage devices.

Experimental Section

Pulsed Laser Deposition Targets: The powders, $\text{Gd}_{0.1}\text{Ce}_{0.9}\text{O}_{2-\delta}$ (Praxair, Woodinville, WA) and Er_2O_3 (Sigma-Aldrich, Switzerland), were uniaxially and then isostatically pressed at 440 bars for 2 min to form ceramic targets. Sintering was carried out isothermally at 1650 °C for Er_2O_3 and at 1400 °C for $\text{Gd}_{0.1}\text{Ce}_{0.9}\text{O}_{2-\delta}$ with hold times of 24 h for Er_2O_3 and of 4 h for $\text{Gd}_{0.1}\text{Ce}_{0.9}\text{O}_{2-\delta}$. Heating and cooling rates were 5 °C min^{-1} each.

Pulsed Laser Deposition Thin Film Fabrication: Mono- and heterolayer film depositions were carried out on round single crystalline, double-side polished (0001)-oriented sapphire substrates (Stettler sapphire,

Switzerland). Before deposition, the PLD chamber (Surface Technologies, Germany; KrF excimer laser, 248 nm) was pumped to a pressure of 4×10^{-6} mbar. The deposition was performed at 700 °C, at an oxygen pressure of 0.0267 mbar, and with a target–substrate distance of 85 mm. The laser energy during deposition was kept constant at 0.81 J cm^{-2} . To get different layer thicknesses the number of pulses was adjusted accordingly, for growth rates see Section S1 (Supporting Information).

Microdot Heterostructure and Sideways Contact Microfabrication: After thin film deposition carried out by pulsed laser deposition, the samples were subjected to photolithography to create a pattern of dots on the films that can be used to make the microdots. Those dots are the template for the microdots. This pattern was made with spin-coating AZ 4533 Photoresist (Microchemical, Germany) to achieve a thickness of 4.3–4.6 μm . After letting the sample rest and soft-bake it at 100 °C for 90 s the sample was exposed in a MA6 mask aligner (SUSS MicroTec, Germany) with a dose of 190 mJ cm^{-2} at 405 nm. After a short resting time the sample was subjected to post-baking at 115 °C for 20 s. After another resting period the sample was developed in two different puddles filled with AZ 826 developer for 39 s in each puddle. Finally, the sample was dried in an N_2 stream. In the next step, the microdots were etched using an Oxford Plasmalab 80. After the dots were free etched the pattern for the electrodes had to be defined. AZ nLoF 2020 (Microchemical, Germany) was spin-coated onto the sample. After a resting period the samples were soft-baked at 110 °C for 180 s followed by another resting period. The samples were exposed with a dose of 75 mJ cm^{-2} at 365 nm. After another resting period they were post-baked at 110 °C for 90 s. After a final resting step for rehydration the samples were developed in two puddles of AZ 726 for 45 s each. Then the samples were dried in an N_2 stream. The details of the fabrication process flow are given in Section S1 (Supporting Information).

Structural Characterization: The ceramic PLD targets and as-deposited thin films were characterized by X-ray Diffraction (Bruker D8, Cu $K\alpha$). Confocal Raman microscopy and Raman mapping (WITec CRM200, WITec, Germany) was done using a 532 nm wavelength laser for excitation with a spectral resolution of 0.7 cm^{-1} . Fitting was done by OriginPro 9.1 using a Gaussian function.

Microstructural Characterization: Scanning electron microscopy (SEM, LEO 1530) was used to analyze the surface topography and cross sections. Preparation of the TEM lamellas was performed using focused ion beam (FIB) scanning electron microscope (Zeiss NVision 40). The gallium beam-induced deposition of the protection layer and then subsequent milling were carried out at 30 kV and 300 pA. HRTEM images were acquired using an FEI Tecnai F30 FEG operating at 300 kV. The annular dark field STEM images were recorded using a FEI Talos F200X operated at 200 kV. Fourier diffractogram analysis was performed using the Gatan DigitalMicrograph software package.

Electrical Measurements and Microdot Device Characterization: Device contacting was done using Pt needles and 3D micropositioners (Everbeing, Taiwan). All electrical measurements were carried out with a Keithley 2612B source measurement unit (Keithley Instruments, USA). Performing was performed using a positive voltage of 200 V with a ramping-up speed of 1 V s^{-1} . After reaching the maximum voltage a compliance current level of 200 nA was set. Previous experiments showed that a current higher than 200 nA can lead to device failure. Performing was successful if the current reached the set compliance level of 200 nA and stayed there until the hold time of 1 h ended. Cyclic voltammetry was carried out with maximum amplitudes of ± 200 V with a sweep rate of 500 mV s^{-1} . Each sample was cycled at least 50 times to ensure stability.

DFT Calculations: The density functional theory calculations were performed with the VASP code^[55] using the PBEsol exchange-correlation functional.^[56] Wavefunctions were expanded in planewaves up to a kinetic energy of 500 eV for PAW potentials^[57,58] with explicit Ce 4f states, while Er 4f states were frozen in the core in an Er^{3+} configuration. For the four-atom fluorite unit cell a $12 \times 12 \times 12$ Γ -centered reciprocal space mesh was used, which was reduced to $3 \times 3 \times 3$ for the 96-atom cubic supercell and to $2 \times 2 \times 1$ for the cell used to describe the $\text{CeO}_2/\text{Er}_2\text{O}_3$ interface. In the calculations, Gd doping was implicitly included

by removing an O atom along with two electrons from the simulation cell when creating an oxygen vacancy, which electronically mimics the presence of a $2\text{Gd}_{\text{Ce}}^{\cdot}$ [V_O] cluster. Phonon calculations were carried out within the frozen phonon method implemented in the Phonopy code.^[59]

Supporting Information

Supporting Information is available from the Wiley Online Library or from the author.

Acknowledgements

The authors acknowledge support of ScopeM/Swiss Federal Institute of Technology ETHZ, particularly from Fabian Gramm and Alla Sologubenko. Support by FIRST cleanroom is kindly acknowledged. The authors want to thank Yanuo Shi for help with the preparation of the FIB lamella. This work was supported by the Swiss National Science Foundation under the Project Nos. 155986 (SNSF (ERC) starting grant) and 138914. W.J.B. acknowledges the use of ASU's John M. Cowley Center for High Resolution Electron Microscopy. W.J.B. was a Swiss Government Excellence Scholarship holder for the academic year 2015–2016 (ESKAS No. 2015.1183) and would like to acknowledge financial support of the U.S. National Science Foundation's Graduate Research Fellowship Program (Grant No. DGE-1311230), as well as the U.S. N.S.F.'s Graduate Research Opportunities Worldwide grant.

Received: September 19, 2016
Published online:

- [1] N. Sata, K. Eberman, K. Eberl, J. Maier, *Nature* **2000**, 408, 946.
- [2] C. Korte, J. Keppner, A. Peters, N. Schichtel, H. Aydin, J. Janek, *Phys. Chem. Chem. Phys.* **2014**, 16, 24575.
- [3] B. Yildiz, *MRS Bull.* **2014**, 39, 147.
- [4] S. Sanna, V. Esposito, J. W. Andreasen, J. Hjelm, W. Zhang, T. Kasama, S. B. Simonsen, M. Christensen, S. Linderth, N. Pryds, *Nat. Mater.* **2015**, 14, 500.
- [5] K. Wen, W. Lv, W. He, *J. Mater. Chem. A* **2015**, 3, 20031.
- [6] A. Fluri, D. Pergolesi, V. Roddatis, A. Wokaun, T. Lippert, *Nat. Commun.* **2016**, DOI: 10.1038/ncomms10692.
- [7] Y. Shi, A. H. Bork, S. Schweiger, J. L. M. Rupp, *Nat. Mater.* **2015**, 14, 721.
- [8] R. Waser, R. Dittmann, G. Staikov, K. Szot, *Adv. Mater.* **2009**, 21, 2632.
- [9] C. O. Park, J. W. Fergus, N. Miura, J. Park, A. Choi, *Ionic* **2009**, 15, 261.
- [10] J. A. Kilner, M. Burriel, *Annu. Rev. Mater. Res.* **2014**, 44, 365.
- [11] J. Santiso, M. Burriel, *J. Solid State Electrochem.* **2011**, 15, 985.
- [12] S. Sanna, V. Esposito, A. Tebano, S. Licocchia, E. Traversa, G. Balestrino, *Small* **2010**, 6, 1863.
- [13] R. A. De Souza, A. Ramadan, S. Horner, *Energy Environ. Sci.* **2012**, 5, 5445.
- [14] International Technology Roadmap for Semiconductor Industry (ITRS) 2014 Edition, Emerging research devices, <http://www.itrs2.net> (accessed: April 2016).
- [15] D. Sacchetto, G. De Micheli, Y. Leblebici, *Proc. IEEE* **2012**, 100, 2008.
- [16] D. Sacchetto, P. E. Gaillardon, M. Zervas, S. Carrara, G. De Micheli, Y. Leblebici, *IEEE Circuits Syst. Mag.* **2013**, 13, 23.
- [17] A. Beck, J. G. Bednorz, C. Gerber, C. Rossel, D. Widmer, *Appl. Phys. Lett.* **2000**, 77, 139.
- [18] J. C. Hou, S. S. Nonnenmann, W. Qin, D. A. Bonnell, *Adv. Funct. Mater.* **2014**, 24, 4113.
- [19] F. Messerschmitt, M. Kubicek, S. Schweiger, J. L. M. Rupp, *Adv. Funct. Mater.* **2014**, 24, 7448.
- [20] A. Wedig, M. Luebben, D. Y. Cho, M. Moors, K. Skaja, V. Rana, T. Hasegawa, K. K. Adepalli, B. Yildiz, R. Waser, I. Valov, *Nat. Nanotechnol.* **2016**, 11, 67.
- [21] M. Kubicek, R. Schmitt, F. Messerschmitt, J. L. M. Rupp, *ACS Nano* **2015**, 9, 10737.
- [22] R. Schmitt, M. Trassin, M. Weber, A. Rossi, M. Fiebig, J. L. M. Rupp, unpublished.
- [23] S. Schweiger, M. Kubicek, F. Messerschmitt, C. Murer, J. L. M. Rupp, *ACS Nano* **2014**, 8, 5032.
- [24] A. Peters, C. Korte, D. Hesse, N. Zakharov, J. Janek, *Solid State Ionics* **2007**, 178, 67.
- [25] C. Korte, A. Peters, J. Janek, D. Hesse, N. Zakharov, *Phys. Chem. Chem. Phys.* **2008**, 10, 4623.
- [26] M. Mogensen, N. M. Sammes, G. A. Tompsett, *Solid State Ionics* **2000**, 129, 63.
- [27] J. L. M. F. Rupp, E. D. Marrocchelli, J.-W. Han, D. Chen, E. Traversa, H. L. Tuller, B. Yildiz, *Adv. Funct. Mater.* **2014**, 24, 1562.
- [28] Y. Y. Zhu, S. Chen, R. Xu, Z. B. Fang, J. F. Zhao, Y. L. Fan, X. J. Yang, Z. M. Jiang, *Appl. Phys. Lett.* **2006**, 88, 162909.
- [29] L. Z. A. Younis, D. Chu, S. Li, *Appl. Phys. Lett.* **2016**, 108, 033506.
- [30] C. C. Hsieh, A. Roy, A. Rai, Y. F. Chang, S. K. Banerjee, *Appl. Phys. Lett.* **2015**, 106, 173108.
- [31] P. A. Crozier, R. G. Wang, R. Sharma, *Ultramicroscopy* **2008**, 108, 1432.
- [32] K. Usuda, T. Mizuno, T. Tezuka, N. Sugiyama, Y. Moriyama, S. Nakaharai, S. Takagi, *Appl. Surf. Sci.* **2004**, 224, 113.
- [33] W. J. Bowman, J. Zhu, R. Sharma, P. A. Crozier, *Solid State Ionics* **2015**, 272, 9.
- [34] J. Kreisel, M. C. Weber, N. Dix, F. Sanchez, P. A. Thomas, J. Fontcuberta, *Adv. Funct. Mater.* **2012**, 22, 5044.
- [35] F. Giannici, G. Gregori, C. Aliotta, A. Longo, J. Maier, A. Martorana, *Chem. Mater.* **2014**, 26, 5994.
- [36] See Section S5 (Supporting Information) for calculation of the Raman spot resolution.
- [37] R. Korobko, C. T. Chen, S. Kim, S. R. Cohen, E. Wachtel, N. Yavo, I. Lubomirsky, *Scr. Mater.* **2012**, 66, 155.
- [38] W. H. Weber, K. C. Hass, J. R. McBride, *Phys. Rev. B* **1993**, 48, 178.
- [39] R. Loudon, *Adv. Phys.* **1964**, 13, 423.
- [40] I. DeWolf, *Semicond. Sci. Technol.* **1996**, 11, 139.
- [41] M. J. Suess, R. A. Minamisawa, R. Geiger, K. K. Bourdelle, H. Sigg, R. Spolenak, *Nano Lett.* **2014**, 14, 1249.
- [42] S. Narayanan, S. R. Kalidindi, L. S. Schadler, *J. Appl. Phys.* **1997**, 82, 2595.
- [43] N. Yavo, D. Noiman, E. Wachtel, S. Kim, Y. Feldman, I. Lubomirsky, O. Yeheskel, *Scr. Mater.* **2016**, 123, 86.
- [44] G. A. Kourouklis, A. Jayaraman, G. P. Espinosa, *Phys. Rev. B* **1988**, 37, 4250.
- [45] A. Sawa, *Mater. Today* **2008**, 11, 28.
- [46] S. Schweiger, W. Bowman, J. L. M. Rupp, unpublished.
- [47] P. Gao, Z. Z. Wang, W. Y. Fu, Z. L. Liao, K. H. Liu, W. L. Wang, X. D. Bai, E. Wang, *Micron* **2010**, 41, 301.
- [48] K. P. Song, H. Schmid, V. Srot, E. Gilardi, G. Gregori, K. Du, J. Maier, P. A. van Aken, *APL Mater.* **2014**, 2, 032104.
- [49] D. S. Aidhy, B. Liu, Y. W. Zhang, W. J. Weber, *J. Phys. Chem. C* **2014**, 118, 30139.
- [50] W. C. Chueh, A. H. McDaniel, M. E. Grass, Y. Hao, N. Jabeen, Z. Liu, S. M. Haile, K. F. McCarty, H. Bluhm, F. El Gabaly, *Chem. Mater.* **2012**, 24, 1876.
- [51] N. V. Skorodumova, S. I. Simak, B. I. Lundqvist, I. A. Abrikosov, B. Johansson, *Phys. Rev. Lett.* **2002**, 89, 166601.

- [52] E. Ruiz-Trejo, G. Tavizon, H. Garcia-Ortega, *J Electrochem Soc* **2007**, *154*, A70.
- [53] E. Ruiz-Trejo, J. Maier, *J Electrochem Soc* **2007**, *154*, B583.
- [54] R. Ortega-Hernandez, M. Coll, J. Gonzalez-Rosillo, A. Palau, X. Obradors, E. Miranda, T. Puig, J. Sune, *Microelectron. Eng.* **2015**, *147*, 37.
- [55] G. Kresse, *J. Non-Cryst. Solids* **1995**, *193*, 222.
- [56] J. P. Perdew, A. Ruzsinszky, G. I. Csonka, O. A. Vydrov, G. E. Scuseria, L. A. Constantin, X. Zhou, K. Burke, *Phys. Rev. Lett.* **2008**, *100*, 136406.
- [57] P. E. Blochl, *Phys. Rev. B* **1994**, *50*, 17953.
- [58] G. Kresse, D. Joubert, *Phys. Rev. B* **1999**, *59*, 1758.
- [59] A. Togo, F. Oba, I. Tanaka, *Phys. Rev. B* **2008**, *78*, 134106.
-

ADVANCED MATERIALS

Supporting Information

for *Adv. Mater.*, DOI: 10.1002/adma.201605049

Designing Strained Interface Heterostructures for Memristive
Devices

*Sebastian Schweiger, Reto Pfenninger, William J. Bowman,
Ulrich Aschauer, and Jennifer L. M. Rupp**

Supporting information to

“Designing Strained Interface Heterostructures for Memristive Devices”

Sebastian Schweiger, Reto Pfenninger, William J. Bowman, Ulrich Aschauer, Jennifer L.M. Rupp*

S. Schweiger Electrochemical Materials, ETH Zürich, Switzerland

R. Pfenninger Electrochemical Materials, ETH Zürich, Switzerland

W.J. Bowman Electrochemical Materials, ETH Zürich, Switzerland and
School for Engineering of Matter, Transport and Energy, Arizona State
University, Tempe, AZ 85287, USA and

Laboratory for Electrochemical Interfaces, Massachusetts Institute of
Technology, 77 Massachusetts Ave., Cambridge, MA, 02139

Prof. Dr. U. Aschauer Materials Theory, ETH Zürich, 8093, Zürich, Switzerland and
Department of Chemistry and Biochemistry, University of Bern, 3012 Bern,
Switzerland

Prof. Dr. J.L.M. Rupp Electrochemical Materials, ETH Zürich, Switzerland
HPP P 21, Hönggerberggring 64, 8093 Zürich, Switzerland
Laboratory for Electrochemical Interfaces, Massachusetts Institute of
Technology, 77 Massachusetts Ave., Cambridge, MA, 02139

* Correspondence should be addressed to J.L.M.Rupp (jrupp@mit.edu)

Supporting information S1: Fabrication details

Compared to the state-of-the-art in literature^[1] we were able to decrease the size of the devices by ~one order of magnitude. After thin film deposition in a PLD system (**Figure S1.1**, step 1), see **Table S1.1** for deposition rates, the samples were subject to a first photolithography step. This photoresist pattern was made with spin-coating AZ 4533 Photoresist (Microchemical, Germany) to achieve a

thickness of 4.3 – 4.6 microns. After letting the sample rest and soft-bake with 100°C for 90 sec the sample was exposed in a MA6 mask aligner (SUSS MicroTec, Germany) with a dose of 190mJ/cm² at 405 nm (**Figure S1.1**, step 2). After resting the sample was post-baked with 115°C for 20 sec. After another resting period we developed the sample in 2 different puddles filled with AZ 826 developer with 39 sec in each puddle. Subsequently the sample was dried in an N₂ stream.

Then the microdots were subject to dry-etching using an Oxford Plasmalab 80 (**Figure S1.1**, step 3). The etching rates for the oxides and the photoresist were measured in previously carried out pilot experiments, see **Table S1.2**. AZ nLoF 2020 was spin-coated onto the sample to create a pattern for metal deposition (**Figure S1.1**, step 4). Following a resting step the samples were soft-baked at 110°C for 180 sec followed by another resting period. The samples were then exposed at 365 nm with a dose of 75 mJ/cm². Another resting period was followed by a post-bake at 110°C for 90 sec. After a final rehydration the samples were developed in 2 puddles of AZ 726 for 45 sec each. The samples were dried in an N₂ stream and finally subject to metal deposition to fabricate the electrodes (**Figure S1.1**, step 5).

A process flow chart depicting the sample fabrication is shown in **Figure S1.1**.

Table S1.1: Thin film deposition rates

Material	PLD deposition rate / nm*100pulses ⁻¹
Er ₂ O ₃	~1
Gd _{0.1} Ce _{0.9} O _{2.8}	~2

Table S1.2: Etch rates

Material	Etch rate in Ar plasma / nm*min ⁻¹
Er ₂ O ₃	0.59

$\text{Gd}_{0.1}\text{Ce}_{0.9}\text{O}_{2-\delta}$	1.24
Sapphire	1.75
AZ nLof 2020	~10

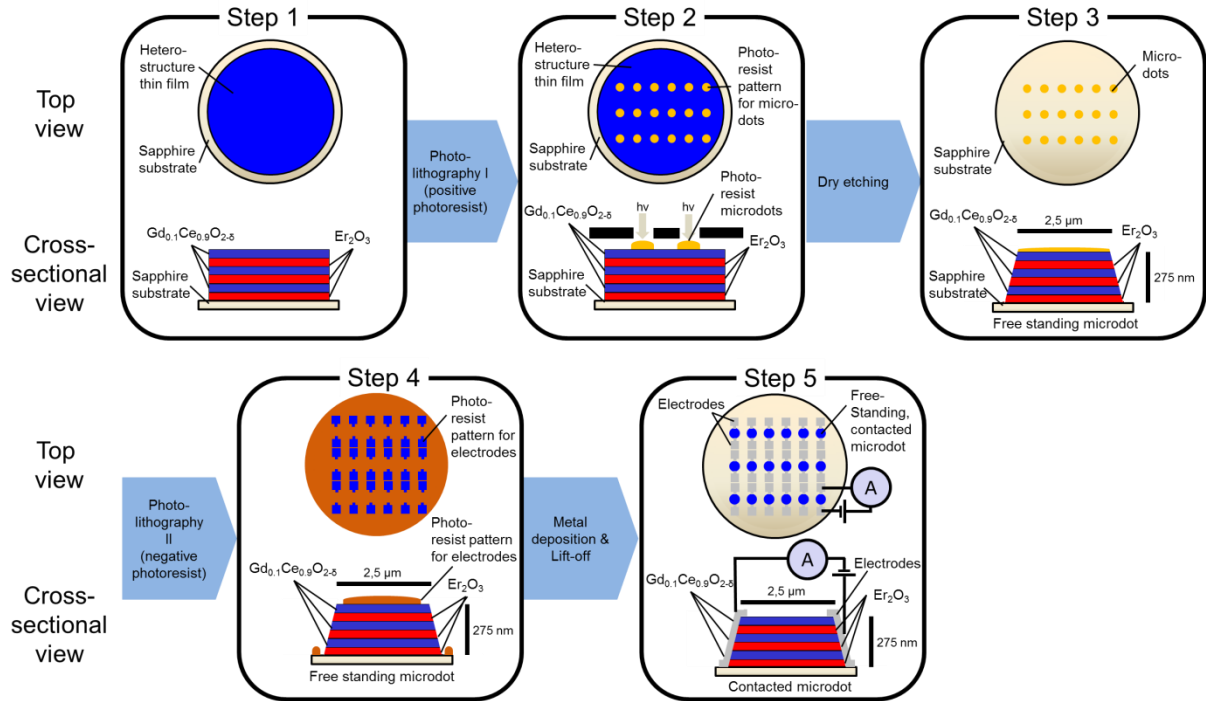


Figure S1.1: Microfabrication process flow to produce strained microdots contacted by electrodes for small dot sizes down to 2.5 microns in diameter.

Supporting information S2: HRTEM diffractogram analysis

Relative assessment of lattice spacing out-of-plane (111) and in-plane (311) was performed *via* Fourier analysis of atomic-resolution images of the 6 and 60 interface samples. Representative [101] zone axis diffractograms computed from $\text{Gd}_{0.1}\text{Ce}_{0.9}\text{O}_{2-\delta}$ in the 60 and 6 interface samples are shown in **Figure S2.1a and b**, respectively. Spot separation was measured 4 to 6 times (typically 5) depending on the number of high order reflections visible in the diffractogram. Standard error propagation was performed using the measured mean and standard deviation.

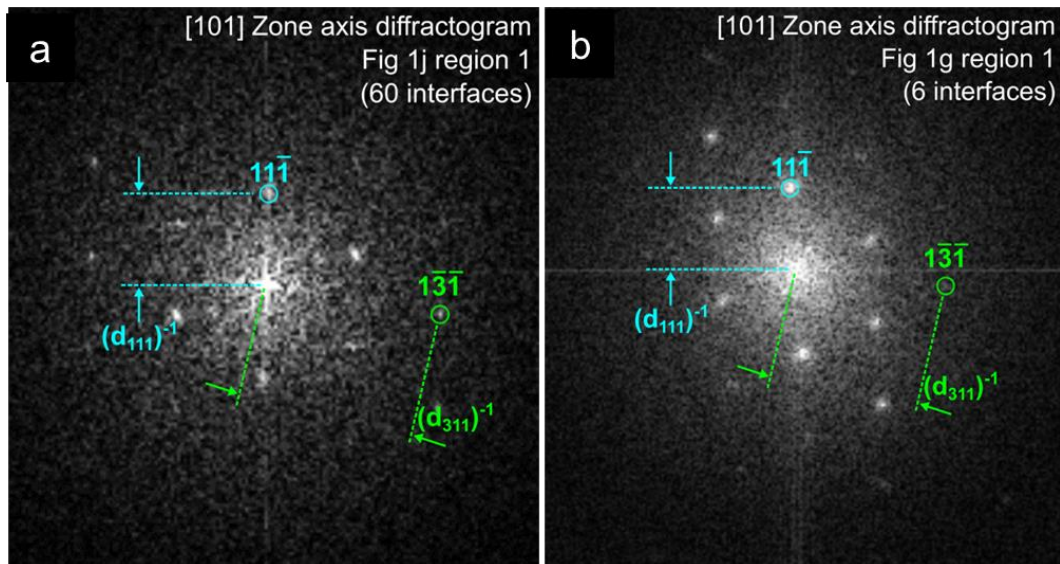


Figure S2.1: Typical [101] zone axis (ZA) diffractograms used for relative lattice plane spacing analysis.

Diffractograms were computed from $\text{Gd}_{0.1}\text{Ce}_{0.9}\text{O}_{2.6}$ layers 60 and 6 interface samples.

The result of this analysis is detailed in **Table 1**, and reveals a relative contraction of the in-plane (311) spacing by $2.8 \pm 0.2\%$ when comparing regions 1 and 2 in the 6 interface sample, **Figure 1h**. This result suggests the strain field relaxes within the several nanometers directly adjacent the interface.

Supporting information S3: XRD Structural characterization

The thin films were also characterized with X-Ray Diffraction in Bragg-Brentano configuration, **Figure S3.1**. The 6 interfaces sample shows the single peaks for both materials, $\text{Gd}_{0.1}\text{Ce}_{0.9}\text{O}_{2-\delta}$ and Er_2O_3 . The 40 and 60 interfaces samples exhibit supelattice modulation.

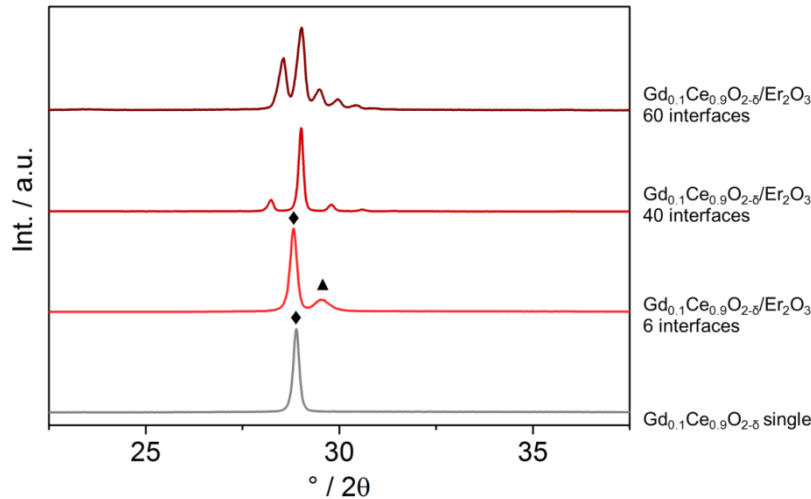


Figure S3.1: X-Ray diffractograms of the thin film samples. The diamond symbol refers to $\text{Gd}_{0.1}\text{Ce}_{0.9}\text{O}_{2-\delta}$ phase and the triangle symbol to Er_2O_3 .

Supporting information S4: Scanning transmission electron microscope electron energy-loss spectroscopy

Dopant cation segregation at the interfaces was investigated in non-preformed samples using STEM EELS to track the intensity ratio of the Ce M_{45} and Gd M_{45} ionization edges. A negligible difference in the intensity ratio, $I_{M_{45}}^{\text{Ce}}/I_{M_{45}}^{\text{Gd}}$, was observed when comparing spectra acquired in the GDC layer ($I_{M_{45}}^{\text{Ce}}/I_{M_{45}}^{\text{Gd}} = 11.6 \pm 0.8$) and within 2.5 nm of the interface ($I_{M_{45}}^{\text{Ce}}/I_{M_{45}}^{\text{Gd}} = 11.8 \pm 1.3$). The cited error is one standard deviation in the mean value measured at five locations along the interface. In the interface region (i.e. within 2.5 nm of the interface), cerium reduction was typically observed as a reversal in the Ce M_5 to M_4 peak height ratio, and a slight shift of both peaks towards lower energy-loss.^[2]

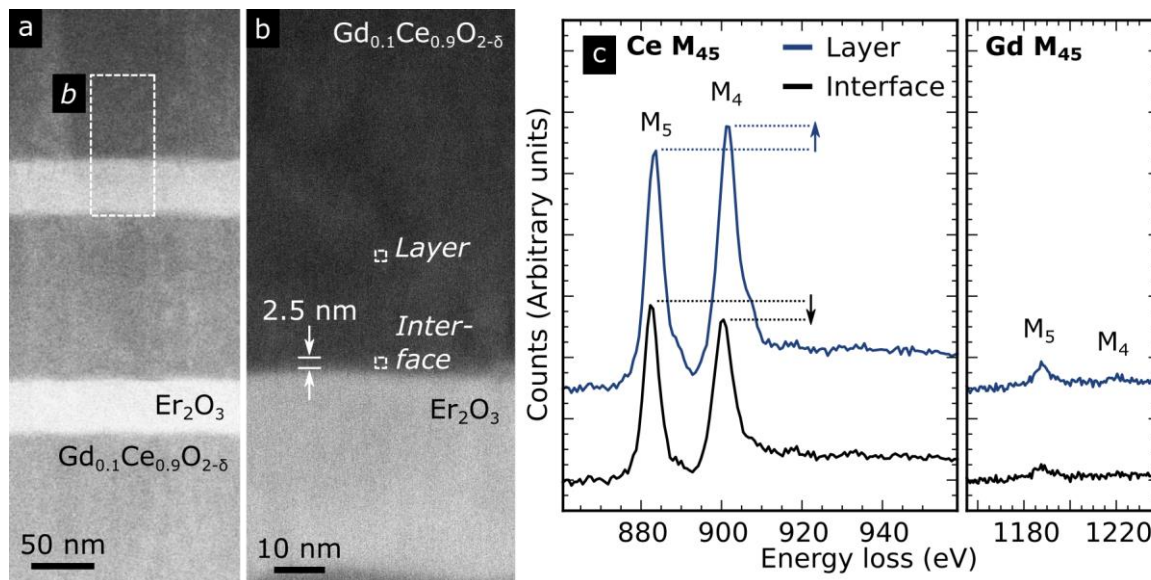


Figure S4.1: **a**, Annular dark field (ADF) STEM image of $\text{Gd}_{0.1}\text{Ce}_{0.9}\text{O}_{2-\delta}/\text{Er}_2\text{O}_3$ 6 interfaces multilayers. **b**, ADF STEM image of a single $\text{Gd}_{0.1}\text{Ce}_{0.9}\text{O}_{2-\delta}/\text{Er}_2\text{O}_3$ interface; the image was acquired in the region of **a** highlighted with a dashed box labeled **b**. **c**, Area-averaged Ce M_{45} and Gd M_{45} energy-loss spectra acquired in the $\text{Gd}_{0.1}\text{Ce}_{0.9}\text{O}_{2-\delta}$ layer 22 nm – 28 nm from the $\text{Gd}_{0.1}\text{Ce}_{0.9}\text{O}_{2-\delta}/\text{Er}_2\text{O}_3$ interface (*Layer*), and acquired within the 2.5 nm directly adjacent to the $\text{Gd}_{0.1}\text{Ce}_{0.9}\text{O}_{2-\delta}/\text{Er}_2\text{O}_3$ interface (*Interface*). The spectra labeled *Layer* and *Interface* were acquired in the regions of **b** highlighted with a dashed box with corresponding labels.

STEM EELS experimental details:

A JEOL 2010F STEM equipped with a Gatan Enfina energy-loss spectrometer was operated with an acceleration voltage of 200 kV. The probe size at the specimen was approximately 0.7 - 1 nm. Individual spectra were acquired with an exposure time of 0.5 s, and a spectrometer dispersion of 0.7 eV/channel. The convergence and collection semi-angles were about 15 mrad and 33 mrad, respectively. For spectral processing, spectra were shifted such that the Ce M_5 edge maxima had an energy loss of 883 eV. An inverse power-law fit to the background signal was used for background subtraction, and signal integration windows were selected to minimize specimen thickness effects (e.g. plural scattering artifacts).^[3] Background fitting and signal integration windows are provided in the table below.

	Background fitting (eV)	Signal integration (eV)
Ce M ₄₅	890 – 870	875 – 955
Gd M ₄₅	1070 – 1170	1175 – 1255

Supporting information S5: Additional Raman Theory

According to Ganesan et al.,^[4] the frequencies of the three optical modes can be described by the following secular equation:

$$\begin{bmatrix} p\varepsilon_{11} + q(\varepsilon_{22} + \varepsilon_{33}) - \lambda & 2r\varepsilon_{12} & 2r\varepsilon_{13} \\ 2r\varepsilon_{12} & p\varepsilon_{22} + q(\varepsilon_{33} + \varepsilon_{11}) - \lambda & 2r\varepsilon_{23} \\ 2r\varepsilon_{13} & 2r\varepsilon_{23} & p\varepsilon_{33} + q(\varepsilon_{11} + \varepsilon_{22}) - \lambda \end{bmatrix} = 0 \text{ Equation (S1)}$$

, where p , q and r are the phonon deformation potentials. The Raman frequencies for the strained and unstrained cases can be calculated from the eigenvalues λ .

$$\lambda = \omega_{strained}^2 - \omega_{unstrained}^2 \text{ Equation (S2)}$$

This can be rewritten as

$$\Delta\lambda = \omega_{strained} - \omega_{unstrained} \approx \frac{\lambda_{strained}}{2\omega_{unstrained}}. \text{ Equation (S3)}$$

Resolution:

The spatial resolution achievable with optical microscopy is given by

$$\text{Spatial resolution} = \frac{0.61 * \lambda}{NA} \text{ Equation (S4)}$$

λ is the wavelength, in this case 532 nm, NA stands for the numerical aperture, which is for the given case 0.9, giving a spatial resolution of about 360 nm on average.

Supporting information S6: Raman Microscopy on Erbia

A Raman spectrum of an Er_2O_3 thin film on sapphire is presented in **Figure S5.1**. All Raman band assignments presented in **Table S5.1** were assigned using Refs. 5-8. A pilot experiment with varying laser powers was conducted to exclude influence from laser-induced sample heating.

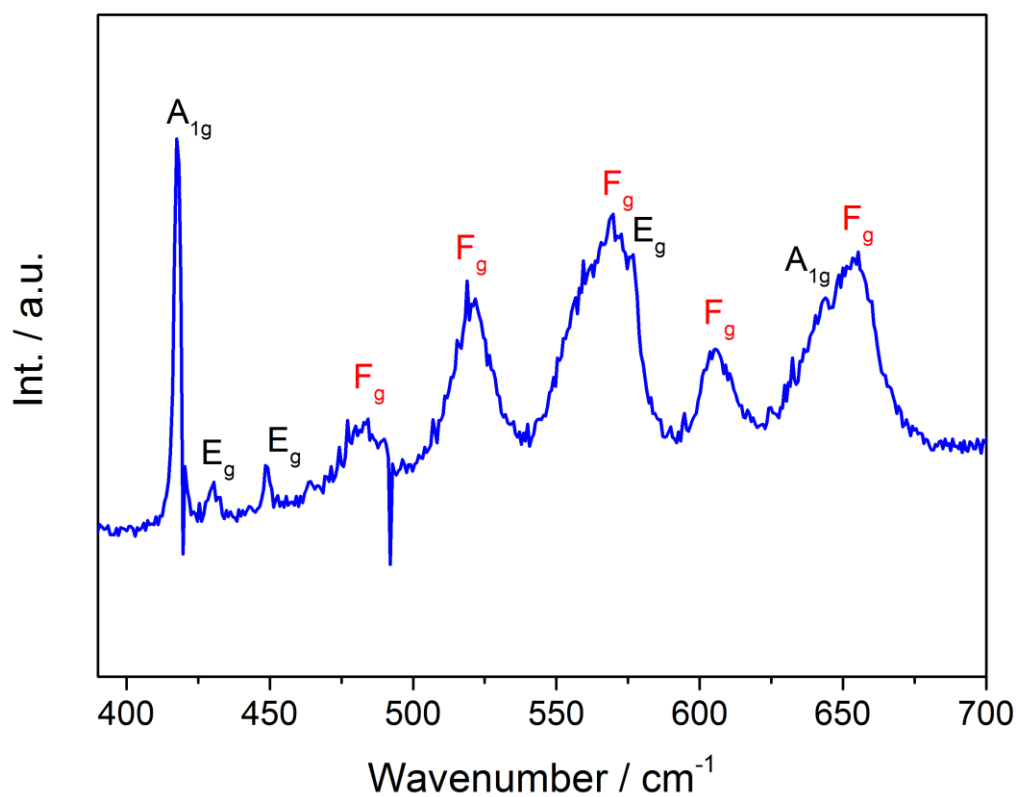


Figure S6.1: Er_2O_3 micro-Raman spectrum. The black indices refer to sapphire vibrational modes and the red denoted indices refer to the phase of Er_2O_3 .

Table S6.1: Assignment of Raman modes for Fig. S5.1 Er₂O₃ micro-Raman spectrum

Wavenumber / cm ⁻¹	Mode	Ref.
~417	A _{1g}	[8]
~430	E _g	[8]
~449	E _g	[8]
~480	F _g	[5-7]
~520	F _g	[5-7]
~569	F _g	[5-7]
~576	E _g	[8]
~605	F _g	[5-7]
~645	A _{1g}	[8]
~655	F _g	[5-7]

Supporting information S7: DFT calculations of vacancies at the CeO₂/Er₂O₃ interface

In **Figure 5c** (main text) we show the energy for oxygen vacancies at different positions in a CeO₂/Er₂O₃ heterostructure. In this calculation, charged oxygen vacancies were created by removing two electrons from the calculation, which mimics the presence of two Gd³⁺ dopants at Ce⁴⁺ sites. The effective composition is thus Gd_{0.06}Ce_{0.94}O_{1.97}.

The disorder in Er₂O₃ leads to a significant scatter in the data, but since high energy states will not be populated, we can focus on the low-energy states highlighted in red. These data points show that vacancies can reside in lower energy states close to the interface, which is in agreement with previous calculations for charged and neutral oxygen vacancies.^[9]

Figure S7.1 reports the oxygen vacancy migration barrier in CeO₂ under applied biaxial strain, for migration along both the in-plane and out-of-plane direction.

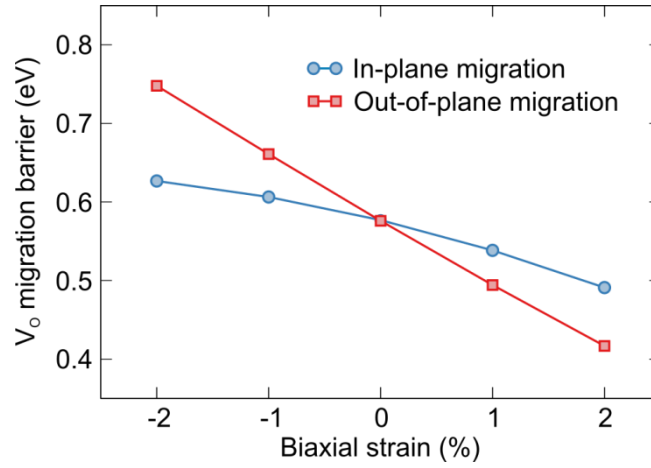


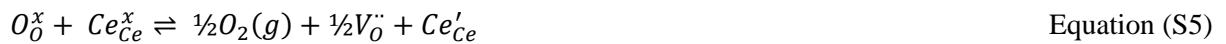
Figure S7.1: Oxygen vacancy migration barriers in CeO₂ under biaxial strain.

Independent of the migration direction, the migration barrier increases under compressive (negative) biaxial strain, which will reduce the mobility of oxygen vacancies under compressive strain.

Figure 5d (main text) shows the bottom of the conduction band of pure CeO₂ around the X (0.0, 0.0, 0.5) point of the Brillouin zone. These bands, which will be occupied by oxygen vacancy-generated electrons, show a systematically higher curvature with increasing compressive strain, which translates to a smaller effective mass and hence a higher mobility of these electrons with increasing strain.

Supporting information S8: Defect chemical equations

The equilibrium at the ceria-erbia interface can be described as follows in Kröger-Vink notation:



References

- [1] S. Schweiger, M. Kubicek, F. Messerschmitt, C. Murer, J. L. M. Rupp, *Acs Nano* 2014, 8, 5032.
- [2] W. J. Bowman, J. Zhu, R. Sharma, P. A. Crozier, *Solid State Ionics* 2015, 272, 9.
- [3] R. F. Egerton, *Electron energy-loss spectroscopy in the electron microscope*, Springer, New York 2011.
- [4] S. Ganesan, Maradudi.Aa, J. Oitmaa, *Ann Phys-New York* 1970, 56, 556.
- [5] M. V. Abrashev, N. D. Todorov, J. Geshev, *J Appl Phys* 2014, 116.
- [6] N. Dilawar, S. Mehrotra, D. Varandani, B. V. Kumaraswamy, S. K. Haldar, A. K. Bandyopadhyay, *Mater Charact* 2008, 59, 462.
- [7] G. Schaack, Koningst.Ja, *J Opt Soc Am* 1970, 60, 1110.
- [8] S. P. S. Porto, R. S. Krishnan, *J Chem Phys* 1967, 47, 1009.
- [9] D. S. Aidhy, B. Liu, Y. W. Zhang, W. J. Weber, *J Phys Chem C* 2014, 118, 30139.